ORIGINAL ARTICLE

An empirical tool for predicting the presence or absence of coseismic displacements at GNSS stations

Demián D. Gómez[1] · Michael G. Bevis[1] · Dana J. Caccamise II[1,2] · W. Ashley Griffith[1] · Jacob M. Heck[1,3] · Robert Smalley Jr[4]

Abstract

Unmodeled displacements in GNSS times series, induced by instrumental artifacts or geophysical events, create significant biases in station trajectory parameters that can propagate into the reference frame itself. While non-tectonic 'jumps', such as equipment changes, affect only a specific GNSS station, seismically-induced displacements can affect large numbers of sites, severely threatening the frame's stability. Manually reviewing individual GNSS time series for such effects is highly impractical because there can be thousands of GNSS stations in a frame, and the total number of earthquakes $Mw \geq 6.0$ since GPS became fully operational is $+5100$. To avoid this time-consuming task, automated methods rely on empirical power-law functions to determine which earthquake-station pairs require coseismic displacement parameters. Still, 'conservative' power-law functions tend to add coseismic offsets to stations that do not need them, which can also threaten the stability of the frame. In this work, we present an empirical formulation that was obtained using 809 global seismic events to fit power-law parameters that do not overestimate the region of influence of earthquakes. Our method is based on a two-level selection process: level 1 is isotropic and only considers the epicentral distance between the stations and the earthquake, and level 2 uses the geophysical parameters of the earthquake to predict a 'tighter' displacement pattern to select which stations require coseismic trajectory parameters. We applied our level 2 method to a database of ~4700 event-station pairs and showed that it removed ~55% of the total pairs, all of which had been falsely selected by level 1.

Introduction

Global GNSS networks providing open data have grown from a few hundred sites with continuously operating stations in the early 1990s to over 20,000 stations that we know of today. There are many more GNSS stations given that there are additional sites which are intermittently-occupied for survey campaigns as well as sites with continuously operating stations whose data are 'closed' or private and not available to the scientific community. This enormous quantity of data is processed daily and used for scientific, engineering, mapping, and many other applications. Automation and unsupervised algorithms are required to process this vast quantity of GNSS data to avoid long delays in generating the products derived from the GNSS observations. This automation includes schemes to identify the times and amplitudes of discontinuities or 'jumps' in the coordinate time series caused by earthquakes, volcanic events, or engineering modifications such as the change of an antenna or its radome. In this paper, we focus on the problem of determining a priori whether an earthquake of known magnitude, location, source time, and fault parameters is likely to have produced a significant coseismic displacement at any or all GNSS stations operating in the same region.

Differential or 'inner coordinate' GNSS solutions are stacked (sometimes along with other observation techniques, see Altamimi et al. 2023) and aligned using a set

✉ Demián D. Gómez
gomez.124@osu.edu

[1] Division of Geodetic Science, School of Earth Sciences, The Ohio State University, Columbus, OH, USA

[2] National Geodetic Survey, National Oceanic and Atmospheric Administration, La Jolla, CA, USA

[3] National Geodetic Survey, National Oceanic and Atmospheric Administration, Ann Arbor, MI, USA

[4] Center for Earthquake Research and Information, The University of Memphis, Memphis, TN, USA

of conventions to realize geodetic reference systems. An important aspect of frame realization is the modeling of coseismic displacements, since unmodeled offsets at GNSS stations can generate significant biases in network trajectory models (Bevis and Brown 2014) and, therefore, in the frame itself. Incorporating coseismic displacements in station trajectory models (Bevis et al. 2020), which can reach over 15 m (Rodgers and Little 2006) and deform thousands of square km, is a non-trivial task given the great amount of GNSS stations and seismic events worldwide. As of this time, there have been more than 5,100 global seismic events of $Mw \geq 6.0$ since 1990 that can potentially generate coseismic displacements that, if unmodeled, will produce biased trajectory models, *reference frame realization errors* (Dietrich et al. 2001; Bevis and Brown 2014) and even disrupt operational GNSS satellite orbit determinations. Identifying which stations or geographical areas suffered coseismic displacements is also important for determining trajectory prediction models used in operational geodesy and land surveying (Gómez et al. 2015, 2023).

The simplest method to determine whether or not one needs to consider co- and postseismic terms in a station's trajectory model is to use a small circle centered on the earthquake's epicenter with a radius based on the earthquake's magnitude. For example, the Nevada Geodetic Laboratory (NGL, Blewitt et al. 2018) uses a power-law function based on the moment magnitude of the earthquake to determine the radius of a small circle that delimits its area of influence. The Geodesy and Geodynamics group at Ohio State University (OSU) also uses a power-law expression, which has been fine-tuned, for reasons that will be explained below, using our own GNSS processing (Bevis and Brown 2014; Caccamise 2019). A significant issue with this power-law method, however, is that it tends to be somewhat 'conservative' in that it includes coseismic step functions at stations that, as we will show, do not need them. This can be seen by noting that any coseismic displacement field has a pattern that is not circular about the epicenter, and a small circle based on the most distant observable displacement will include large areas with no deformation.

Adding co- and postseismic terms to stations that were not affected by an earthquake can degrade the stability of a frame, especially when the frame is realized by combining regional GNSS network solutions (e.g., Gómez et al. 2022). Many (and probably most) of the sites that fit coseismic parameters, but do not need them, will 'find' them, *i.e.* they will not find displacements equal to zero due to correlated noise and other effects. When these trajectory models are used for reference frame realization, they will degrade its quality. Furthermore, biases in the GNSS trajectory models can leak into downstream products that use the time series parameters as input. Hence, an accurate, automatic, method to predict which GNSS stations should include co- and postseismic parameters is required to avoid the need for analyst intervention for potentially many stations.

We present here an improved method to determine if coseismic terms are required in a GNSS station's trajectory model that is not solely based on the epicentral location and moment magnitude, but also the earthquake's focal mechanism. The focal mechanism describes the fault and the movements on it (slip) that together with standard elastic modeling can be used to predict the surface deformation pattern from any earthquake, and we will use this to provide an improved definition of the area to include the coseismic trajectory terms. We will first obtain a new set of power-law parameters based on a less conservative determination of the small circle's radius, which has been fine-tuned using 809 earthquakes, and that we call 'Level 1' (L1). We then develop an improved coseismic deformation predicted pattern, that we call 'Level 2' (L2), calculated using a uniform half-space (Okada 1985) with dislocation dimensions obtained from simple empirical formulations (Wells and Coppersmith 1994) and the earthquake's focal mechanism. L2 uses the results from L1 for a first cut selection, adding a true–false mask based on the calculated far-field surface displacements. We applied our methodology to the entire OSU GNSS coseismic database and show that our method successfully predicts which stations suffer coseismic displacements based solely on the USGS National Earthquake Information Center (NEIC, Masse and Needham 1989) hypocenter and moment tensor solutions.

Data and methods

The OSU GNSS archive contains ~6000 global stations, totaling ~14 M station-days from GNSS networks such as the International GNSS Service (IGS), the *Instituto Geográfico Militar Uruguay*, the United States National Geodetic Survey, the *Instituto Brasileiro de Geografia e Estatística*, the *Centro Sismológico Nacional*, Chile (Báez et al. 2018), and the *Red Argentina de Monitoreo Satelital Continuo* (Piñón et al. 2018) to mention just a few (see Data Availability). This large network was processed using double differences (DD) in GAMIT/GLOBK v10.71 (Herring et al 2008) and a parallelized Python wrapper known as Parallel. GAMIT (Gómez 2017). Processing of GPS data used the orbits and antenna calibration parameters available from the IGS14 reference frame, the Vienna Mapping Functions (Boehm et al. 2006) to estimate the atmospheric delays, and the ocean tide loading model FES2014b (Lyard et al. 2020). The DD technique is known for its solutions' low noise level compared to other techniques, such as Precise Point Positioning (PPP). Thus, our DD solutions facilitate the detection of small station displacements which are important for the determination of the L1 power-law parameters.

To compute the GNSS station trajectory models, we use an automated procedure and the GNSS displacement time series following Bevis and Brown (2014) and Bevis et al. (2020). The automation process includes the automatic incorporation of GNSS periodic components (whenever it is possible to fit these parameters) and mechanical displacements produced by equipment changes. The determination of the trajectory models also requires prior knowledge of the time of displacements generated by seismic events. This work describes in detail the methodology used to determine which earthquakes affect any given GNSS station.

## Determination of the power-law parameters for Level 1

Using our latest global solution we initially adopted the a priori power-law values from NGL that provide a maximum earthquake epicentral distance below which trajectory models of GNSS stations require the incorporation of co- and postseismic parameters. Therefore, the maximum epicentral distance in km, d_{max}, to consider coseismic displacements produced by an earthquake with moment magnitude Mw can be calculated as

$$d_{max} = 10^{(a \cdot Mw + b)} \tag{1}$$

where the a priori parameters are $a = 0.5$ and $b = -0.79$, adopted from NGL. To give two examples using (1), GNSS

stations within ~5700 km of a Mw 9.1 earthquake would require coseismic displacement parameters, as will stations within ~4000 km of a Mw 8.8 event. Based on our experience, these distances are overestimates, so these parameters can be considered conservative. In other words, more stations will be required to fit coseismic parameters than are needed.

Using (1), we computed the trajectory models for all stations within d_{max} for 809 global earthquakes with Mw $\geq$ 6 (see Supplementary Information S1 for more details about the seismic events), resulting in 4700 earthquake-GNSS station pairs with coseismic displacements. Here, we will use GNSS data only and, therefore, 'earthquake-station pair' denotes a coseismic displacement parameter fit for a GNSS station. Figure 1a shows the magnitude of the coseismic displacements as a function of epicentral distance colored by event magnitude. Figure 1b shows the same dataset, displaying moment magnitude instead of displacement in the y-axis. Because the power-law parameters used in (1) overestimate d_{max}, there are far-field stations with spurious coseismic displacements for earthquakes that they did not sense or observe. Thus, we wish to find new parameters for (1) that minimize the number of far-field stations identified as requiring coseismic step functions. We do this by setting a lower observable displacement limit of 1 mm, slightly below an optimistic noise floor for GNSS data, marked as a horizontal dashed line in Fig. 1a, and selecting all event-station displacements below this threshold. Using only the
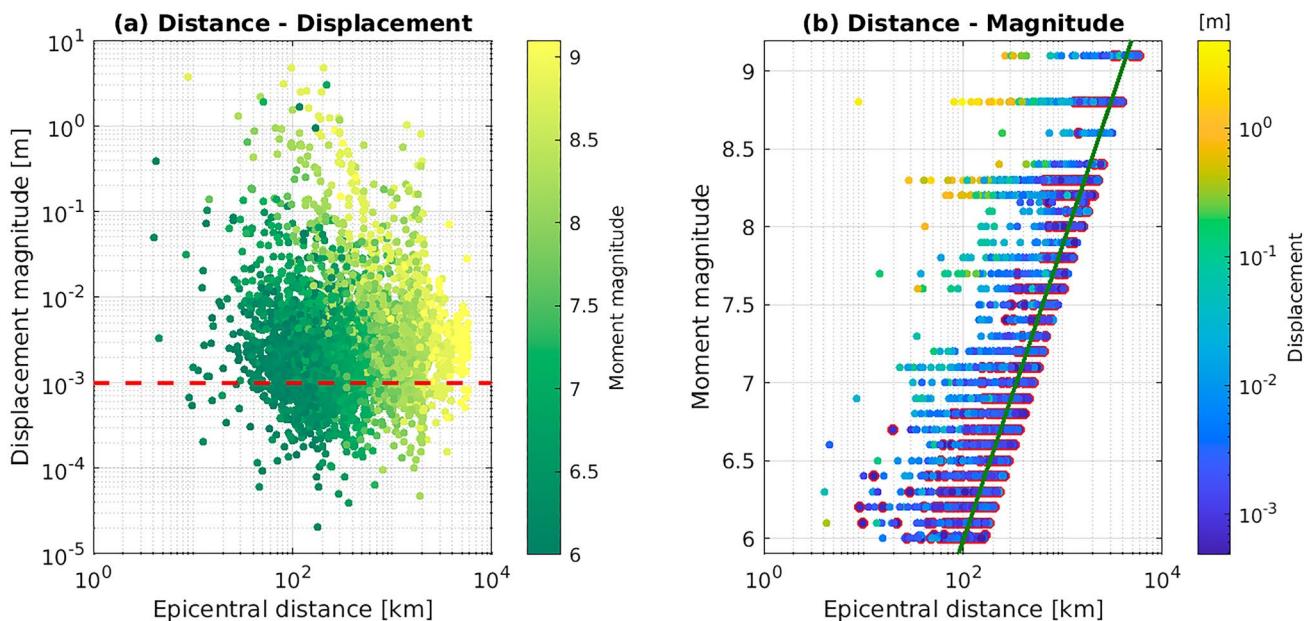
Fig. 1 Coseismic data used to improve the power-law parameters. **a** Displacement magnitude as a function of epicentral distance. Colors represent the earthquake's moment magnitude. The horizontal dashed line is the upper limit for selecting data to fit the power-law param-

eters. **b** Moment magnitude as a function of epicentral distance. Colors represent the displacement magnitude. Observations below the dashed line in **a** are highlighted in red. The slanted solid line is the weighted least squares fit to the highlighted observations

data below this limit, we obtain a new fit for the parameters a and b in (1) while weighting the observations by $10^{2 \cdot (Mw-6)}$ to account for the lower number of large-magnitude events. The new fit is shown in Fig. 1b as a green solid line ($a = 0.526$ and $b = -1.148$). We note some displacements with magnitude > 1 mm beyond the new limit. Still, these are the result of bad fits or noisy data (*i.e.*, far from the epicentral area, we expect displacements with low signal-to-noise ratio).

Using this new fit, we now introduce a subtle modification to the power-law function to simplify interpreting the results from (1). Taking log_{10} on both sides of (1) and rearranging yields

$$0 = 0.526 \cdot Mw - log_{10}(d_{max}) - 1.148 \qquad (2)$$

The right-hand side of (2) is ≤ 0 when the epicentral distance is $\geq d_{max}$, and > 0 when the distance is < d_{max}. Thus, we define the 'seismic score' or simply the 'S-score' as

$$S = 0.526 \cdot Mw - log_{10}(d) - 1.148 \qquad (3)$$

where d is a GNSS station's epicentral distance. When S is > 0 for a given earthquake, a station should include the co- and postseismic parameters for the event and not include them if S is ≤ 0.

Figure 2a shows the data from Fig. 1b but as a function of the S-score defined in (3), where we note that the data on the right side of the power-law line in Fig. 1b shows S-score values that are ≤ 0. From the original 4700 station-earthquake

pairs, we now identified 3761 as having possible displacements, while the improved L1 S-score rejected the remaining 939 earthquake-station pairs. The rejected event-station pairs represent a 20% reduction of the total dataset. As an example of the improvement of the S-score in predicting which stations can record a coseismic displacement, we take two stations identified by the a priori S-score as containing coseismic displacements from the Mw 6.4 Jan 18, 2021, San Juan, Argentina earthquake (Oro et al. 2023). The time series for GNSS station Jáchal, San Juan, Argentina (JCHL), shown in Fig. 2b, does not show identifiable horizontal displacements (the vertical was removed from the plot for clarity and due to the absence of signals). Our improved L1 S-score < 0 correctly predicts that the event did not affect the station, as seen in Fig. 2b. In contrast, Fig. 2c shows that GNSS station Reserva Don Carmelo, San Juan, Argentina (RDCM) (the vertical was removed from the plot for clarity and due to the low signal-to-noise ratio) was correctly identified by both S-scores (a priori and improved). We will later perform a more exhaustive test of the method's capability, including a test for Level 2.

Although, in principle, the L1 S-score parameters show a significant improvement relative to the a priori parameters, the S-score is still based on a small circle as it does not account for the earthquake's surface displacement field pattern. In other words, the L1 S-score provides the same value (for a given earthquake-station pair) for both a thrust or strike-slip event with the same magnitude, despite having
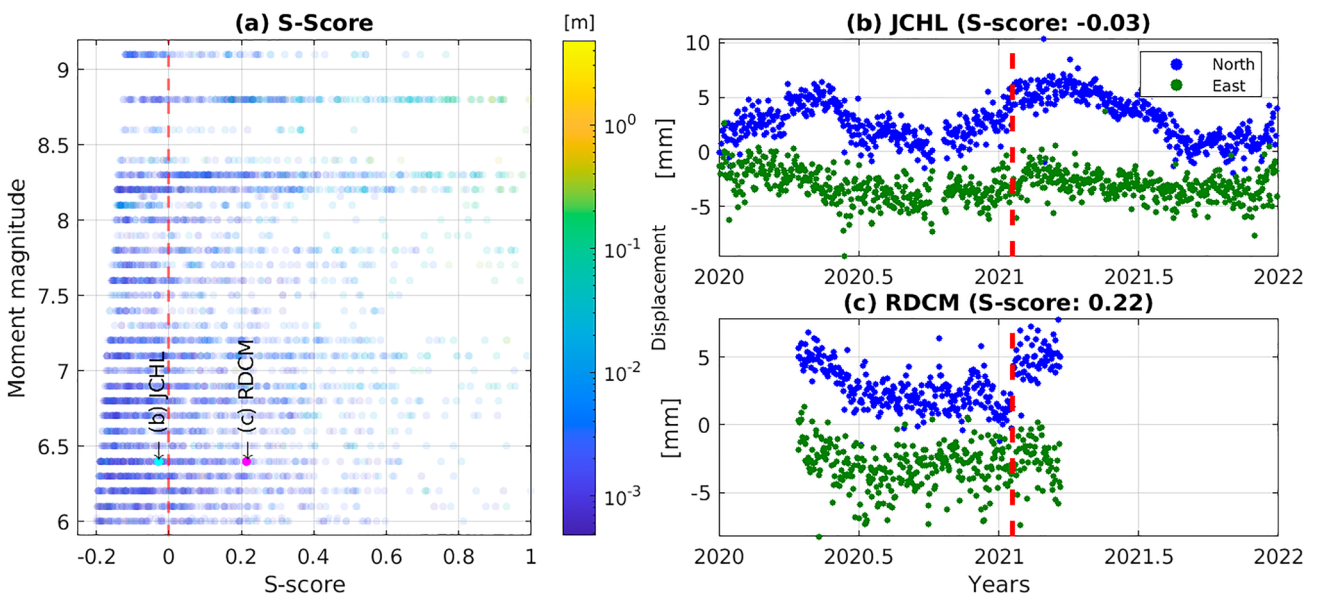
Fig. 2 **a** Moment magnitude displacements as a function of S-score. The vertical dashed line shows the S-score cutoff value. Data points are colored by displacement magnitude. S-score truncated to 1 for clarity. Cyan and magenta dots show the S-score for stations JCHL **b** and RDCM **c**. **b** The time series for GNSS station JCHL lacks coseis-

mic displacements. The red vertical dashed line shows the time of the Mw 6.4 Jan 18, 2021, San Juan, Argentina earthquake. **c** Same as **b** for GNSS station RDCM showing the presence of coseismic displacements, with the red vertical dashed line showing matching that as in **b**

different displacement field patterns. Moreover, the S-score formulation does not consider the events' depth as it only uses the epicentral distance. To resolve these shortcomings, we developed an L2 S-score incorporating information about the 'expected' displacement field predicted by a uniform elastic half-space model, as a function of its focal mechanism and hypocenter's depth.

Level 2: Improvement of the prediction quality of the S-score

There are many formulations used to produce surface elastic deformation due to point or finite fault dislocations (e.g., Pollitz 1996; Wang et al. 2003; Aagaard et al. 2017; Zhou et al. 2020). One of the most commonly used formulations is that of a finite rectangular dislocation embedded in a homogeneous half-space from Okada (1985). Its popularity is mainly due to its simplicity, the availability of the source code, and because it was published as the early GPS results being obtained needed such modeling. Although Okada's formulation fails to capture the effects of the Earth's sphericity, layering, and gravity (Dong et al. 2014; Gómez et al. 2017), it provides a first-order approximation of the expected displacement field due to an earthquake. We aim to compute the approximate displacement field for a seismic event, so the Okada formulation will suffice for this purpose. Therefore, to use Okada we need the properties of the fault (location, strike, and dip) and the movement (rake) of the earthquake on the fault.

The L1 S-score uses the epicentral locations from the USGS NEIC database to compute the earthquake-station distance and is based on criteria using only this distance. Jointly with each event's hypocenter and magnitude, the NEIC database also contains moment tensor solutions that provide the double-couple focal mechanism nodal planes and rakes for most (~ 82%) of the seismic events with Mw $\geq$ 6 since 1994. The focal mechanism data, that provide the strike, dip, and rake, can be used with empirical scaling formulations from Wells and Coppersmith (1994), which provide slip, fault length and width estimates based on Mw (see Appendix A), to provide the needed fault data for Okada, allowing estimation of an earthquake's approximate displacement field. We will describe how the displacement field magnitudes (hereafter $||u||$) can be used to create an S-score 'mask' to predict which stations recorded coseismic displacements for a given earthquake.

Computation of the approximate displacement field

We compute $||u||$ to create a mask as follows: First, we define the fault using the size estimated above and the strike and dip from one of the two focal mechanism nodal planes. We then place the fault's centroid at the event's epicenter, and use the hypocenter location as an initial fault depth, where the Okada Cartesian (x, y, z) coordinate system is aligned with the east, north, and down system at the epicenter. We adjust the depth accordingly if the top of the fault extends outside of the elastic half-space (see Appendix B). Finally, we use Okada to compute $||u||$ out to a distance of ~ 20 × along-strike fault lengths. We note that the $||u||$ field from each nodal plane will be different in the near-field, but they are nearly identical in the far-field, beyond approximately ten fault dimensions, where we make the include or exclude decision for the stations. For completeness, we illustrate this by taking as an example the Mw 6.4 San Juan, Argentina event used in the previous section. Figure 3a–b shows $||u||$ for each nodal plane, where we note their similarity (to zero order). We take the difference between both fields in Fig. 3c, where we note that the differences in $||u||$ beyond ~ 10 fault dimensions are less than 1 mm. This behavior of $||u||$ in the far-field applies to any fault type or hypocentral depth, as observed in Fig. 3d–f, where we show the same as Fig. 3a–c but for the Mw 7.1 Mar 25, 2012 Constitución, Chile, thrust event. Using $||u||$, it is therefore possible to estimate an S-score mask to decide a priori if a station's displacement magnitude is greater or less than 1 mm, providing a more realistic determination than that from the small circle L1 S-score.

L2 S-score mask

We define a minimum observable displacement magnitude of 1 mm and obtain the regions where $||u||$ is above this value (Fig. 3a–c and d–e, white contour). We compute the distance of all points with $||u|| > 1$ mm and search for the point furthest from the origin (hereafter, d, see Fig. 3a–c and d–e, red dot). Finally, a binary true–false mask is found for the event (where $||u|| > 1$ mm = true and false otherwise) by rescaling the Okada coordinate system using the ratio d_{max}/d, where d_{max} is calculated using (1) and its improved parameters. To account for any minor differences between fault plane masks (see Fig. 3d and e), we apply a logical OR operation to combine them, which results in a more conservative mask. To reconcile the Okada distances on a half space with the Earth's spherical geometry, we use an azimuthal equidistant projection (see Appendix C) to convert the Cartesian coordinate system of the mask to latitude and longitude. We apply the mask to the L1 S-score to decide if a GNSS station requires a coseismic step function for a given earthquake. If the L1 S-score is > 0 and the mask is 'true' for the location of the GNSS station, then the station requires a coseismic step function and a postseismic transient in the time series.
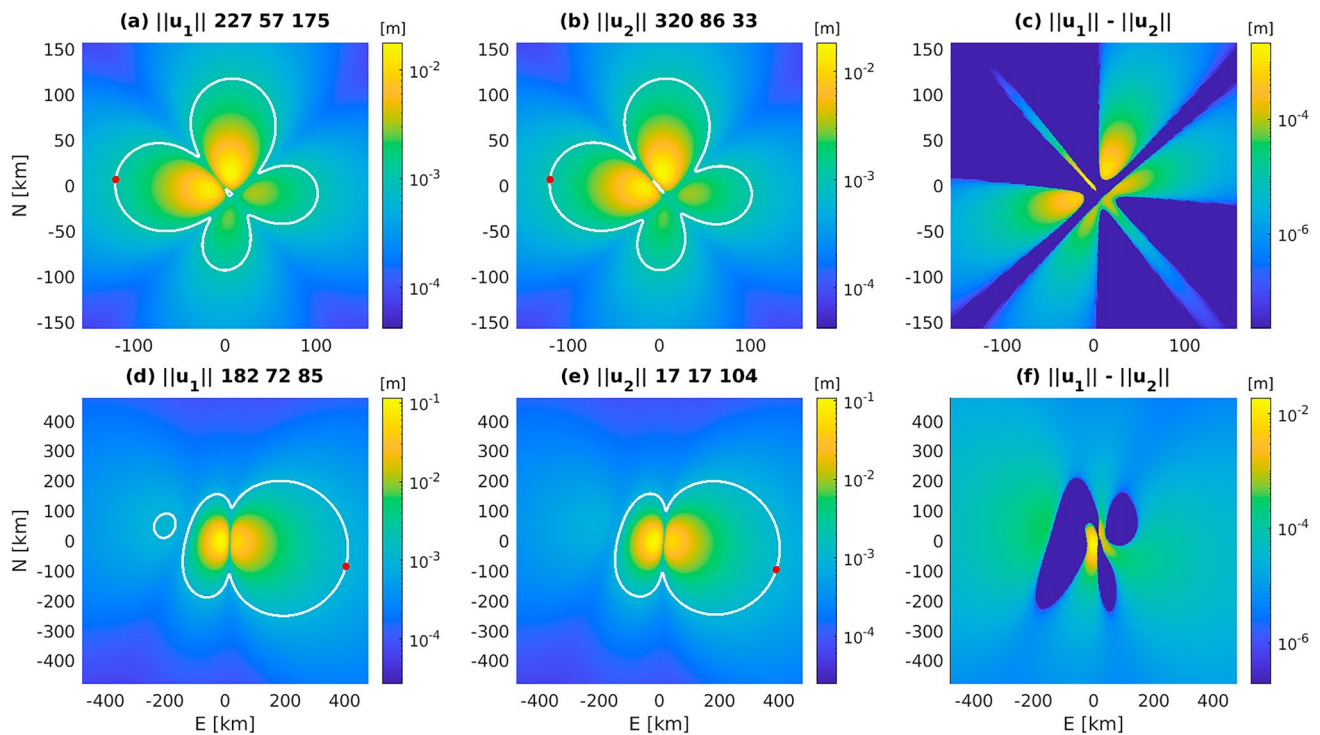
Fig. 3 Displacement field magnitudes and differences for both nodal planes of a single focal mechanism. **a** The displacement field magnitude for the Mw 6.4 Jan 18, 2021, San Juan, Argentina earthquake (nodal plane parameters, strike: 227°, dip: 57°, and rake: 175°) in a Cartesian coordinate system centered on the fault. The white contour shows the location of the 1 mm displacement magnitude. The red dot shows the maximum distance from the coordinate system origin where displacement is ≥ 1 mm. For reference, 10 fault dimensions are ~150 km. **b** Same as **a** for the second nodal plane (strike: 320°,

dip: 86°, and rake: 33°). **c** Difference between **a** and **b**. **d** Same as **a** for the Mw 7.1 Mar 25, 2012, Constitución, Chile earthquake (strike: 182°, dip: 72°, and rake: 85°). For reference, 10 fault dimensions are ~480 km. **e** Same as **d** for the second nodal plane (strike: 17°, dip: 17°, and rake: 104°). We note a small difference in the 1 mm contour on the west side of **d** which is not present in **e**. These differences can be considered by applying an OR operation to the displacement field masks. **f** Differences between **d** and **e**

Accounting for source depth

To account for the effect of source depth, we compute $||u||$ for the shallowest possible source, defined as the shallowest depth where the fault does not outcrop, and the reported source depth. For both fields where $||u|| > 1$ mm, we find the point furthest from the origin, compute d, and rescale the Okada coordinate system, as before, by the scale factor d_{max}/d, this time using the largest distance d of the two depths. This rescaled coordinate system for $||u||$ is used to obtain the final L2 S-score mask. Figure 4 shows a workflow diagram with the steps used to determine the L1 and L2 S-scores.

To demonstrate the ability of the L2 S-score to reject the incorporation of coseismic parameters for deep earthquakes, Fig. 5a shows a deep seismic event, an Mw 6.7 on Feb 11, 2015, with an epicentral distance of 103 km W of El Aguilar, Argentina (depth of ~220 km). In this case, the L1 S-score, represented by the dashed red line in Fig. 5a, identified 88 stations that should have sensed this event. Nevertheless, none of the stations in this area show any discernible

coseismic displacements (Fig. 5b, c shows the two closest continuous GNSS stations). Computing the L2 S-score using the source depth reveals a small area (solid blue line) where GNSS stations can sense this event. We also show the L2 S-score mask for the minimum source depth (dashed blue line) for reference. Notice that GNSS station Casa Quemada, Jujuy, Argentina (CSQM) shows a small apparent displacement of ~2 mm in the north direction. This displacement is, however, unrelated to the seismic event; approximately one month later (marked with a cyan vertical line), another displacement occurred in the opposite direction. Placing a coseismic step function at the day of the event would most likely absorb this offset, incorrectly attributing a coseismic displacement to this earthquake. This example highlights the importance of not incorporating coseismic parameters when they are unnecessary, thus improving the stability of a reference frame realized using these stations.

As an example of other source types, Fig. 6a shows a map view of the L1 and L2 S-score for both source depths (shallowest and USGS catalog depth) of the Mw 6.4 Jan 18, 2021, San Juan, Argentina event. We note that the shallowest
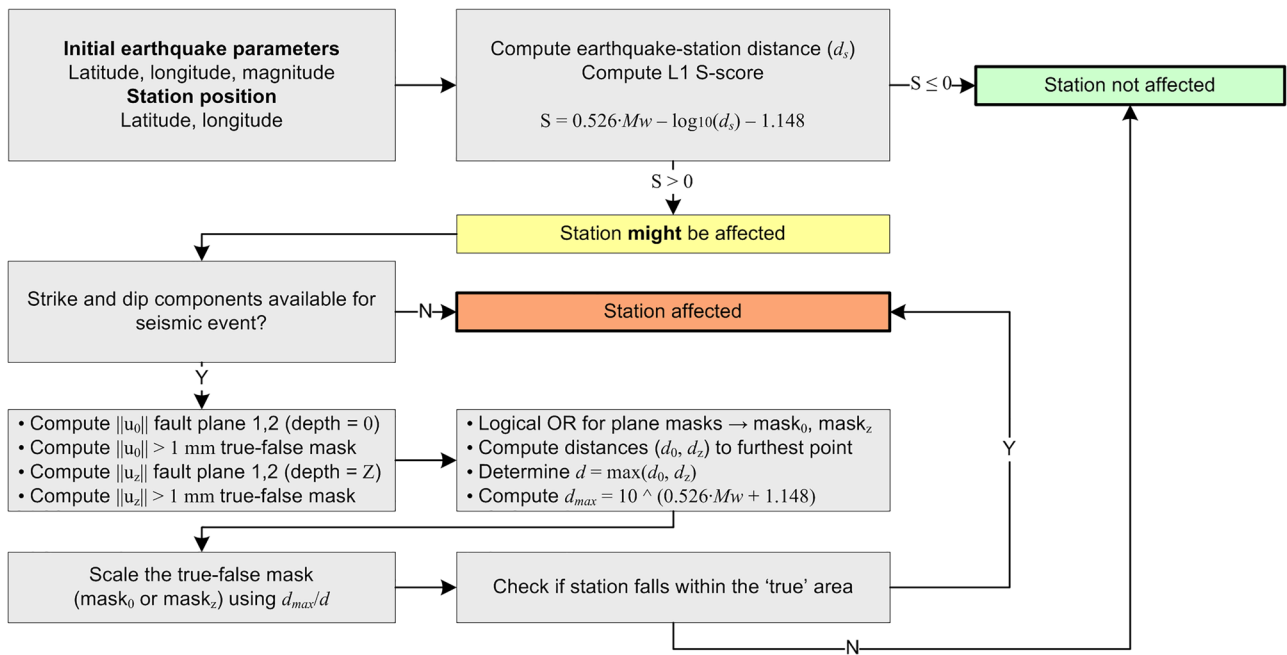
Fig. 4 Workflow of the L1 and L2 S-scores used to determine if a GNSS station can sense or not a specific seismic event
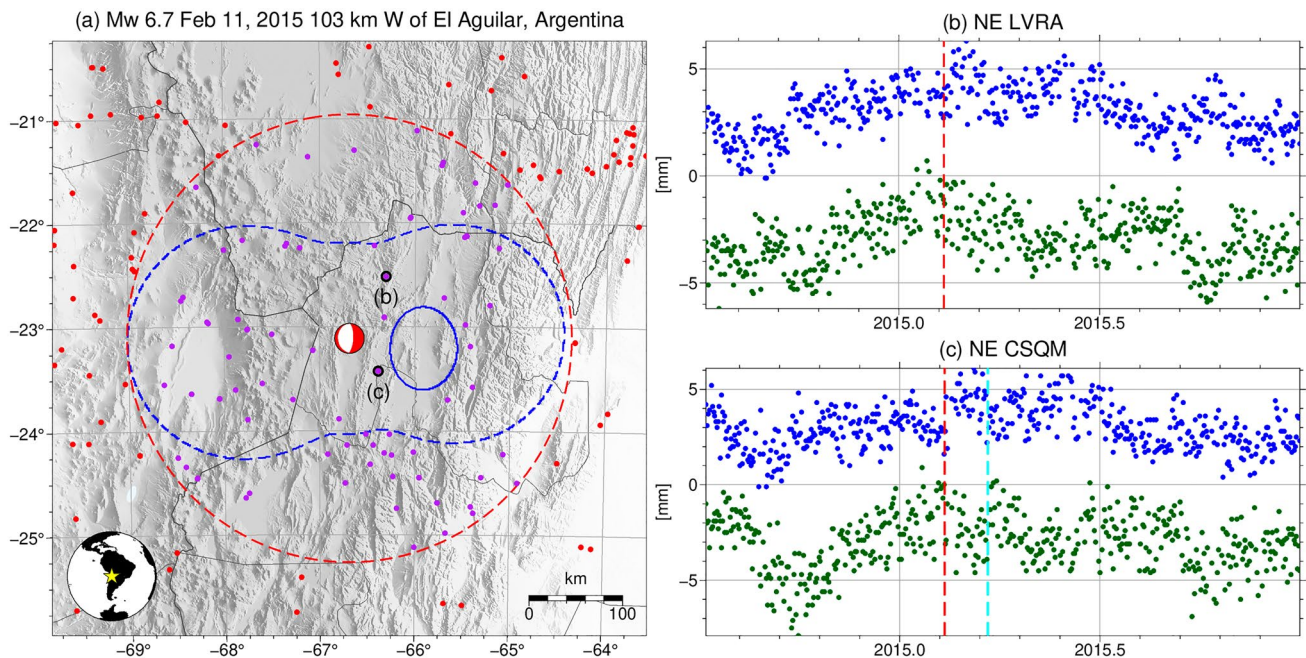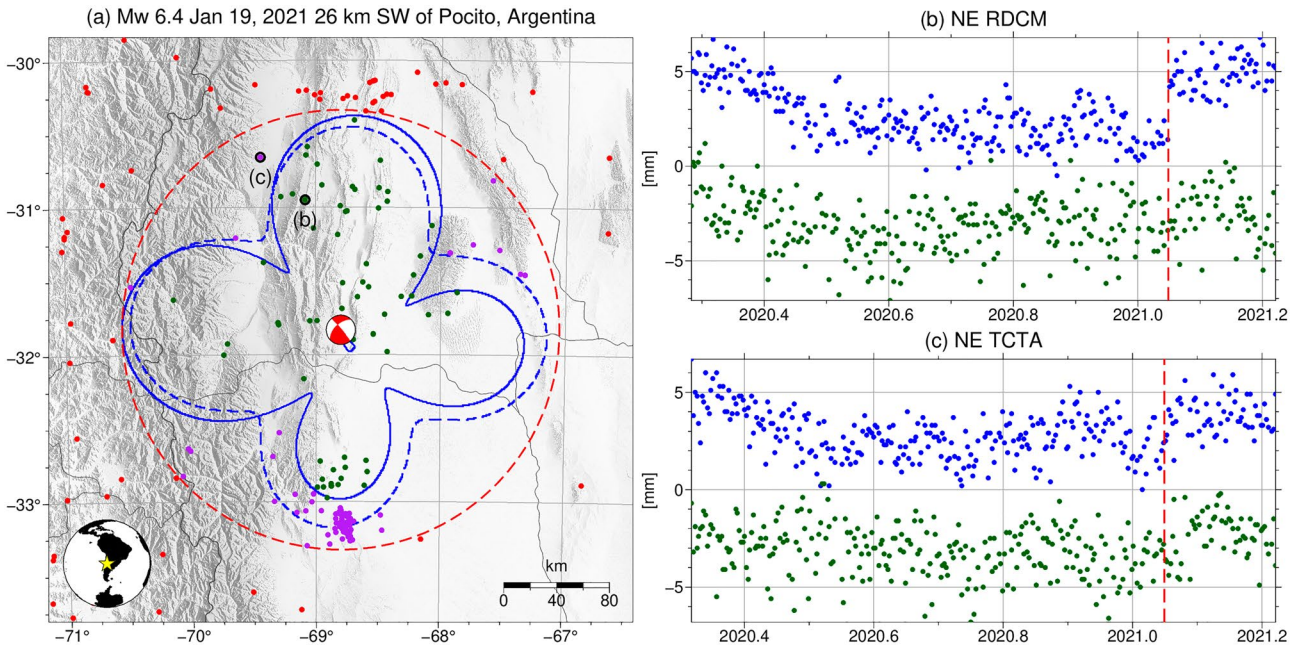

Fig. 5 Map view of the Mw 6.7 Feb 11, 2015, 103 km W of El Aguilar, Argentina earthquake. **a** Focal mechanism marking location of event, GNSS stations, L1 (dashed red line), and L2 S-scores (solid, for the catalog source depth, and dashed for shallowest possible depth, blue lines). The solid blue line shows the area where positive detections could occur, but there are no stations there. Red dots: GNSS stations outside the L1 S-score. Purple dots: GNSS stations inside the L1 S-score but with L2 S-score = false. Stations Liviara, Jujuy, Argentina (LVRA) and Casa Quemada, Jujuy, Argentina (CSQM) are highlighted. **b** Time series of station LVRA for north (blue) and east (green) components. The vertical dashed red line shows the time of the event. **c** Same as **b** for station CSQM. We note that an offset is visible in the north component, but this occurs about three days after the event and is therefore unrelated to the earthquake. About a month after the event the solutions appear to show an offset in the opposite direction marked by the vertical cyan line. Figure made using Generic Mapping Tools (Wessel et al. 2019)

Fig. 6 Map view of the Mw 6.4 Jan 19, 2021 San Juan, Argentina earthquake. **a** Focal mechanism marking location of event, GNSS stations, L1 (dashed red line) and L2 S-scores (solid and dashed blue lines). Dashed and solid blue line, red dots, and purple dots, as in Fig. 4a. Green dots: GNSS stations with L2 S-score = true. Stations RDCM and TCTA are highlighted. **b** Time series of station RDCM for north (blue) and east (green) components. The vertical dashed red line shows the time of the event. **c** Same as **b** for station TCTA. Figure made using Generic Mapping Tools (Wessel et al. 2019)

source sometimes creates a mask with a smaller d than that for the reported catalog depth, as observed in this example. This effect depends on the orientation of the fault and its rake. Figure 6b shows the data from a nearby station RDCM (also shown in Fig. 2c) where the coseismic displacement is visible. Figure 6c shows that station Tocota, San Juan, Argentina, (TCTA, ~ 50 km NW from RDCM and outside the L2 mask) does not show a coseismic displacement for the event. The Supplementary Information section presents several other selected earthquakes (Figs. S3–S8).

If the user wishes to use a more conservative approach than the L2 S-score mask described above, a scale factor can be applied to d_{max} (that may be applied only to specific events) to inflate the S-score and, therefore, expand the limits of the L2 mask.

Results

We tested our L2 S-score approach using 753 events (from the original total of 809) that have focal mechanism solutions. Out of the 753 events, the L1 S-score identified a total of 2,544 earthquake-station pairs. After applying the L2 S-score, we reduced the number of identified earthquake-station pairs to 1,238, representing a 51% reduction, meaning that 1,306 earthquake-station pairs were unselected by the L2 S-score. To verify that we did not fail to predict

coseismic displacements at some GNSS stations, where the L1 S-score previously predicted a displacement, we stacked 21 days (the day of the event, 10 days before, and 10 days after) of GNSS position magnitudes around the time of the earthquake for all unselected earthquake-station pairs. To stack the observations, we first obtained the average 10-day pre-earthquake detrended position for each earthquake-station pair. We then estimated the magnitude of the north, east, and up differences between the 10-day average and all the positions for the 21 days around the event. Thus, the displacement magnitudes for station i, day $j = (−10, 10)$, and event k were calculated as

$$u_{i,k}^{j} = \sqrt{\left(N_i^j - \widehat{N}_k\right)^2 + \left(E_i^j - \widehat{E}_k\right)^2 + \left(U_i^j - \widehat{U}_k\right)^2} \qquad (4)$$

where $u_{i,k}^{j}$ is the displacement magnitude for day j, $\left(N_i^j, E_i^j, U_i^j\right)$ is the north, east, and up position of station i and day j, and $\left(\widehat{N}_k, \widehat{E}_k, \widehat{U}_k\right)$ are the average north, east, and up positions for event k before the earthquake.

Figure 7a shows a scatter plot of all the displacement magnitudes computed using (4) for stations with L2 S-score = false. The red line shows the average displacement magnitude for all observations, with a slight increase in the average displacement of ~ 2 mm after the events (marked by a vertical dashed line on day 0). We
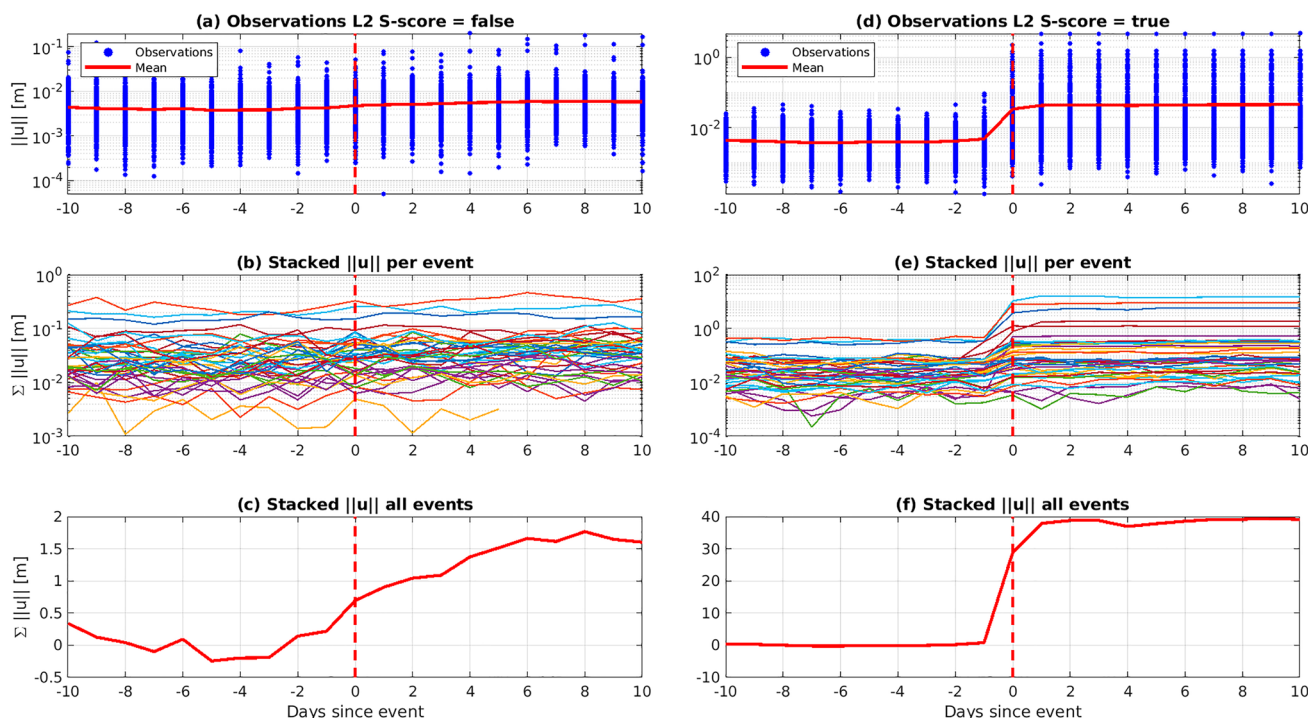
Fig. 7 Stack of the magnitude of GNSS solutions filtered by the L2 S-score mask. **a** Displacement magnitudes relative to the pre-earthquake position (blue dots) for earthquake-station pairs with L2 S-score = false. The solid red line represents the average of the blue dots. The vertical dashed red line shows the time of the events. **b** Stacked displacements per event. Each line represents a different earthquake. **c** The sum of displacement magnitudes for all earthquakes. We note a possible postseismic signal in the stacked time series. **d**, **e** and **f** are the same as **a**, **b**, and **c** except for earthquake-station pairs where L2 S-score = true

grouped the observations by event (for events with more than 20 GNSS stations within the L1 S-score but outside of L2, thus avoiding noisy results) in Fig. 7b, where each line represents the stacked (sum) displacement magnitudes per earthquake. We note no clear tendency in this plot. Finally, Fig. 7c shows the stack of all the observations where we now clearly observe a slow but steady increase in displacement. Comparing these plots against Figs. 7d–f, which show the same as Figs. 7a–c but for stations with L2 S-score = true, we note that a coseismic signal is present. Splitting the maximum stacked displacement equally among stations in the analysis yields an average of ~ 1 mm per event-station when L2 S-score = false, and an average of ~ 4 cm per event-station when L2 S-score = true.

The data in Fig. 7c suggest that while the L2 S-score correctly predicted stations without coseismic displacements, a postseismic component must be accounted for in the GNSS time series even when the L2 S-score is false (and L1 S-score > 0). Predicting postseismic deformation using the S-score, however, is outside the scope of the present work.

Discussion

Using simple formulations, we presented a new approach for empirically predicting which GNSS stations will record coseismic displacements. First, using OSU's extensive GNSS database, we adjusted the parameters of a power-law function (L1 S-score) to obtain an estimate of the maximum small circle distance at which an earthquake of a given moment magnitude can generate displacements detectable with GNSS. Using the L1 S-score, we obtained a robust binary true–false mask to account for the source depth and the nonsymmetric displacement field pattern for the earthquake source parameters (L2 S-score). Our method shows that it is possible to confidently predict which stations will sense (and not sense) an earthquake without failing to detect stations affected by coseismic displacements. From the original 4700 event-station pairs (obtained using the a priori parameters), we reduced the number of positive detections to 2600 (including those using only L1 S-score due to lack of focal mechanisms). This new method requires no supervision by users and

allows automatic incorporation of earthquake coseismic parameters without implementing computationally expensive algorithms. Consequently, mapping agencies realizing reference frames or research groups doing geodynamic modeling can use this method to process massive amounts of GNSS data and obtain sets of reliable earthquake coseismic displacements. Our method also defines a clear, quantitative boundary for the implementation of coseismic deformation models. A working version of the L1 and L2 S-score methodology has been implementation in Parallel.GAMIT (see Python module pyOkada within Parallel.GAMIT).

Our analysis of the L2 S-score tests suggests a postseismic signal in the data with L1 S-score > 0 and L2 = false, although the stations recorded no coseismic displacements. We suggest that this occurred because afterslip is taking place over a larger spatial aperture than coseismic slip, so displacements driven by afterslip decay more slowly with distance than coseismic displacements. These results indicate that another version of the S-score (or scale factor) could be derived to predict the maximum distance at which stations require postseismic transients without invoking coseismic step functions.

Appendix A

Expressions from Wells and Coppersmith (1994) allow computing the fault dimensions and average slip based on the moment-magnitude of an earthquake. We transcribed the following expressions from tables 2A and 2B.

$$
\begin{aligned}
\text{Along} - \text{strike length (km)} &: \quad log_{10}(d_a) = -3.22 + 0.69 \cdot Mw \\
\text{Down} - \text{dip length (km)} &: \quad log_{10}(d_d) = -1.01 + 0.32 \cdot Mw \\
\text{Average slip magnitude (m)} &: \quad log_{10}(s_a) = -4.80 + 0.69 \cdot Mw
\end{aligned}
$$

$$(5)$$

Appendix B

The fault depth for an event is obtained from the hypocentral location and used to compute the minimum and maximum depth of the fault plane for Okada as,

$$
d_{min/max} = d \pm \frac{d_d}{2} \cdot sin(\delta) \tag{6}
$$

where δ is the fault's dip, d is the catalog hypocentral depth (positive down), d_d is the total downdip length as defined by (5) and $d_{min/max}$ are the top and bottom of the event's rupture plane. If $d_{min} < 0$, then the depth of the fault plane definition (d_{new}) is modified as,

$$
d_{new} = d - d_{min} \tag{7}
$$

Appendix C

To convert Cartesian coordinates to latitude and longitude, we find the values of φ, λ from the east (x) and north (y) coordinates using the inverse azimuthal equidistant projection,

$$
\lambda = arctan\left(\frac{x \cdot sin(c)}{\rho \cdot cos(\varphi_0) \cdot cos(c) - y \cdot sin(\varphi_0) \cdot sin(c)} \right) + \lambda_0 \tag{8}
$$

$$
\varphi = arcsin\left(cos(c) \cdot sin(\varphi_0) + \frac{y \cdot sin(c) \cdot cos(\varphi_0)}{\rho} \right) + \varphi_0 \tag{9}
$$

where (φ_0, λ_0) is the latitude and longitude of the origin of the coordinate system (event epicenter), $\rho = \sqrt{x^2 + y^2}$, and $c = \rho/R$ with $R = 6371 km$.

Author contributions All authors contributed to the study's conception and design. Demián D. Gómez and Michael G. Bevis performed material preparation, data collection, and analysis. Demián D. Gómez wrote the first draft of the manuscript, and all authors commented on previous versions. All authors read, commented, and approved the final manuscript.

Data availability Data is public and available through various websites, including the International GNSS Service data repository, the Argentine Instituto Geográfico Nacional, the Chilean Centro Sismológico Nacional, the Instituto Brasileiro de Geografia e Estatística, the Instituto Geográfico Militar Uruguay, the United States National Geodetic Survey, and through the UNAVCO Facility Archive. The code for Parallel.GAMIT is available at GitHub https://github.com/demiangomez/Parallel.GAMIT.

Declarations

Conflict of interest The authors declare no conflict of interest.

References

Aagaard BT, Knepley MG, Williams CA (2017) PyLith v2.2.0. Davis CA Comput Infrastruct Geodyn. https://doi.org/10.5281/zenodo.438705

Altamimi Z, Rebischung P, Collilieux X et al (2023) ITRF2020: an augmented reference frame refining the modeling of nonlinear station motions. J Geod 97:47. https://doi.org/10.1007/s00190-023-01738-w

Báez JC, Leyton F, Troncoso C et al (2018) The Chilean GNSS network: current status and progress toward earlywarning applications. Seismol Res Lett 89:1546–1554. https://doi.org/10.1785/0220180011

Bevis M, Brown A (2014) Trajectory models and reference frames for crustal motion geodesy. J Geod 88:283–311. https://doi.org/10.1007/s00190-013-0685-5

Bevis M, Bedford J, Caccamise DJ II (2020) The art and science of trajectory modelling. In: Montillet J-P, Bos MS (eds) Geodetic Time series analysis in earth sciences. Springer International Publishing, Cham, pp 1–27

Blewitt G, Hammond W, Kreemer C (2018) Harnessing the GPS data explosion for interdisciplinary science. Eos 99:e2020943118. https://doi.org/10.1029/2018eo104623

Boehm J, Werl B, Schuh H (2006) Troposphere mapping functions for GPS and very long baseline interferometry from European centre for medium-range weather forecasts operational analysis data. J Geophys Res Solid Earth. https://doi.org/10.1029/2005JB003629

Caccamise DJ (2019) Geodetic and Oceanographic Aspects of Absolute Versus Relative Sea-Level Change. Ph.D., The Ohio State University

Dietrich R, Dach R, Engelhardt G et al (2001) ITRF coordinates and plate velocities from repeated GPS campaigns in Antarctica—an analysis based on different individual solutions. J Geodesy 74:756–766

Dong J, Sun W, Zhou X, Wang R (2014) Effects of Earth's layered structure, gravity and curvature on coseismic deformation. Geophys J Int 199:1442–1451. https://doi.org/10.1093/gji/ggu342

Gómez D (2017) Parallel.GAMIT (Version 1.0.0) [Computer software]. https://github.com/demiangomez/Parallel.GAMIT

Gómez DD, Piñón DA, Smalley R et al (2015) Reference frame access under the effects of great earthquakes: a least squares collocation approach for non-secular post-seismic evolution. J Geod. https://doi.org/10.1007/s00190-015-0871-8

Gómez DD, Bevis M, Pan E, Smalley R (2017) The influence of gravity on the displacement field produced by fault slip. Geophys Res Lett 44:9321–9329. https://doi.org/10.1002/2017GL074113

Gómez DD, Bevis MG, Caccamise DJ (2022) Maximizing the consistency between regional and global reference frames utilizing inheritance of seasonal displacement parameters. J Geod 96:9. https://doi.org/10.1007/s00190-022-01594-0

Gómez DD, Figueroa MA, Sobrero FS et al (2023) On the determination of coseismic deformation models to improve access to geodetic reference frame conventional epochs in low-density GNSS networks. J Geod 97:46. https://doi.org/10.1007/s00190-023-01734-0

Herring TA, King RW, McClusky SC (2008) Introduction to Gamit/Globk. Mass Inst Technol Camb

Lyard FH, Allain DJ, Cancet M, et al (2020) FES2014 global ocean tides atlas: design and performances. Ocean Sci Discuss 1–40. https://doi.org/10.5194/os-2020-96

Masse RP, Needham RE (1989) NEIC—the National Earthquake Information Center. Earthq Volcanoes USGS 21:4–44

Okada Y (1985) Surface deformation due to shear and tensile faults in a half-space. Bull Seismol Soc Am 75:1135–1154

Oro A, Blanc PA, Colavitto B et al (2023) Surface deformation and secondary effects of the January 18, 2021 (Mw 6.5) San Juan (Argentina) earthquake from remote sensing techniques. Int J Earth Sci 112:2267–2291. https://doi.org/10.1007/s00531-023-02354-x

Piñón DA, Gómez DD, Smalley R et al (2018) The History, state, and future of the argentine continuous satellite monitoring network and its contributions to geodesy in Latin America. Seismol Res Lett 89:475–482. https://doi.org/10.1785/0220170162

Pollitz FF (1996) Coseismic deformation from earthquake faulting on a layered spherical Earth. Geophys J Int 125:1–14

Rodgers DW, Little TA (2006) World's largest coseismic strike-slip offset: The 1855 rupture of the Wairarapa Fault, New Zealand, and implications for displacement/length scaling of continental earthquakes. J Geophys Res Solid Earth. https://doi.org/10.1029/2005JB004065

Wang R, Marítn FL, Roth F (2003) Computation of deformation induced by earthquakes in a multi-layered elastic crust—FORTRAN programs EDGRN/EDCMP. Comput Geosci. 29:195–207

Wells DL, Coppersmith KJ (1994) New empirical relationships among magnitude, rupture length, rupture width, rupture area, and surface displacement. Bull Seismol Soc Am 84:974–1002. https://doi.org/10.1785/BSSA0840040974

Wessel P, Luis JF, Uieda L et al (2019) The generic mapping tools version 6. Geochem Geophys Geosystems 20:5556–5564. https://doi.org/10.1029/2019GC008515

Zhou J, Pan E, Bevis M (2020) A point dislocation in a layered, transversely isotropic and self-gravitating Earth— Part III: Internal deformation. Geophys J Int. https://doi.org/10.1093/gji/ggaa319